

Geometry-Consistent Neural Shape Representation with Implicit Displacement Fields

Wang Yifan
ETH Zurich
yifan.wang@inf.ethz.ch

Lukas Rahmann
ETH Zurich
lrahmann@student.ethz.ch

Olga Sorkine-Hornung
ETH Zurich
sorkine@inf.ethz.ch

Abstract

We present *implicit displacement fields*, a novel representation for detailed 3D geometry. Inspired by a classic surface deformation technique, displacement mapping, our method represents a complex surface as a smooth base surface plus a displacement along the base’s normal directions, resulting in a frequency-based shape decomposition, where the high frequency signal is constrained geometrically by the low frequency signal. Importantly, this disentanglement is unsupervised thanks to a tailored architectural design that has an innate frequency hierarchy by construction. We explore implicit displacement field surface reconstruction and detail transfer and demonstrate superior representational power, training stability and generalizability.

1 Introduction

Neural implicit functions have emerged as a powerful tool for representing a variety of signals. Compared to conventional discrete representations, neural implicits are continuous and thus not tied to a specific resolution. Recently, neural implicits have gained significant attraction in a variety of applications ranging from 3D reconstruction [44, 32, 54, 36], neural rendering [31, 38], image translation [46, 11] to deformation approximation [17]. In this paper, we focus on neural implicit representations for 3D geometry.

While neural implicits can theoretically model geometry with infinite resolution, in practice the output resolution is dependent on the representational power of neural nets. So far, the research community approaches the problem from two main directions. The first is to partition the implicit function using spatial structures [8, 26, 28, 50], thus making the memory and computation demands dependent on the geometric complexity. The other direction focuses on improving networks’ ability to represent high-frequency signals, either in a preprocessing step (referred to as positional encoding) [31] or by using sinusoidal representation networks (SIREN) [45]. However, training these networks is very challenging, as they are prone to overfitting and optimization local minima.

Inspired by the classic computer graphics technique, displacement mapping [15, 16], we propose a novel parameterization of neural implicit functions, *implicit displacement field*, abbreviated as IDF, to circumvent the above issues. Our method automatically disentangles a given detailed shape into a coarse base shape represented as a continuous, low-frequency signed distance function and a continuous high-frequency implicit displacement field, which offsets the base iso-surface along the normal direction.

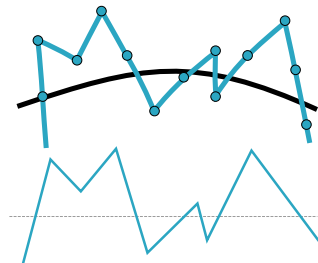


Figure 1: Displacement mapping in 1D. The detailed surface (upper blue) is created by offsetting samples of the base surface (upper black) using the height map shown below.

The key novelty of our approach lies in extending the classic displacement mapping, which is discrete and lies only on the base surface, to a continuous function in the \mathbb{R}^3 domain and incorporating it into contemporary neural implicit representations, ergo achieving a disentanglement of geometric details in an unsupervised manner.

Our main technical contribution includes

1. a principled and theoretically grounded extension of explicit discrete displacement mapping to the implicit formulation,
2. a neural architecture that creates a geometrically interpretable frequency hierarchy in the neural implicit shape representation by exploiting the inductive bias of SIRENS, and
3. introducing transferable implicit displacement fields by replacing the common coordinates input with carefully constructed transferrable features, thus opening up new opportunities for implicit geometry manipulation and shape modeling.

Systematic evaluations show that our approach is significantly more powerful in representing geometric details, while being lightweight and highly stable in training.

2 Related work

Hierarchical neural implicit shape representation. Neural implicit shape representation was initially proposed by several works concurrently [34, 12, 30], and since then many works have sought to introduce hierarchical structures into the neural representation for better expressiveness and generalizability. The majority of these methods focus on spatial structures. DLS [8] and PiFU [42, 43] use sparse regular voxels and dense 2D grid, respectively, to improve detail reconstruction. In the spirit of classic approaches [20, 33], NSVF [28] and NGLOD [50] store learned latent codes in shape-adaptive octrees, leading to significantly higher reconstruction quality and increased rendering speed. A common disadvantage of these methods is that the memory use and model complexity are directly tied to the desired geometric resolution. In parallel, other proposed methods learn the spatial partition. Some of these methods decompose the given shape using parameterized templates, such as anisotropic Gaussians [21], convex shape CVXNet [18, 13] or simple primitives [23], while others represent local shapes with small neural networks and combine them together either using Gaussians [22] or surface patches [52]. Due to limitations of template functions and delicate spatial blending issues, these methods can only handle very coarse geometries.

Concurrently, Li and Zhang [27] propose a two-level neural signed distance function for single-view reconstruction. Exploiting the fact that most man-made shapes have flat surfaces, it represents a given shape as a coarse SDF plus a frontal and rear implicit displacement map for better detail construction. Besides having entirely different applications – we focus on representing significantly higher geometry resolutions – our implicit displacement is grounded in geometry principles and applies to general shapes.

High-frequency representation in neural networks As formally explained in [41, 4], neural networks have a tendency to learn low-frequency functions. To combat this issue, Mildenhall et al. [31] incorporate “positional encoding” for neural rendering and demonstrate remarkable progress in terms of detail reconstruction, which is a sinusoidal mapping for the input signal, a practice later theoretically justified by Tancik et al. [51]. Alternatively, SIREN also shows impressive advances in detail representation by replacing ReLU activation with sin functions. With these new networks gaining popularity, a few works delve deeper and apply a coarse-to-fine frequency hierarchy in the training process for deformable shape representation [35] and meshing [25]. In our method, we also create a frequency hierarchy by leveraging this new form of networks – not only in the training scheme but also explicitly in the construction of the networks to reflect our geometry-motivated design principles.

Detail transfer Detail transfer refers to transplanting the disentangled geometric details from a source shape onto a target object with high fidelity and plausibility. Classic detail transfer methods represent surface details as normal displacements [7, 57, 47]. The majority of them are parametric [56, 6, 48, 58, 49], relying on a consistent surface parameterization between the source and the target shape. Non-parametric approaches [10, 5], on the other hand, find best-matching surface patches

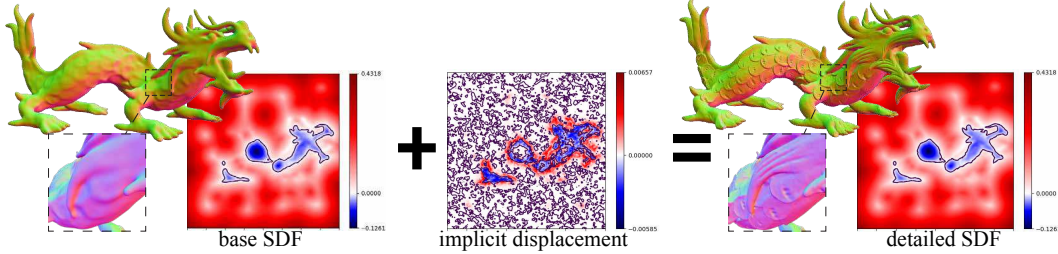


Figure 2: Method overview. We represent detailed geometries as a sum of a coarse base shape represented as low-frequency signed distance function and a high-frequency implicit displacement field, which offsets the base iso-surface along the base’s normal directions.

between the source and target, and copy the details iteratively from coarse to fine. These classic approaches produce high quality results, but often require a pre-defined base surface or abundant user inputs. In the “deep” realm, DeepCage [55] proposed a neural deformation method that maps solely the coarse geometry, hence allowing detail transfer without tackling detail disentanglement. Hertz et al. [24] learn the coarse-to-detail correspondence iteratively from multi-scale training data, while DecorGAN [14] synthesizes details by upsampling a coarse voxel shape according to a style code of another shape using GANs. All of these approaches use explicit representations, hence they are subject to self-intersection and resolution limitations. D²IM-Net [27] uses two planar displacement maps to transfer surface details by mapping the coordinates of the source and target shapes using part segmentation, thus limiting the application to man-made rigid shapes. In comparison, our method does not require any correspondence mapping.

3 Method

We represent a shape with fine geometric details using two SIREN networks of different frequencies in the activation functions. The SIREN with lower frequency describes a smooth base surface; the SIREN with higher frequency adds microstructure to the base iso-surface by producing an implicit displacement field along the base’s normal direction (see Figure 2).

In this section, we first formally define implicit displacement field by generalizing the classic explicit and discrete displacement mapping in Section 3.1, then in Section 3.2 we introduce the network architectures and training strategies that are tailored to this definition, finally in Section 3.3 we extend the implicit displacement to address transferability.

3.1 Implicit displacement fields

In classic displacement mapping as shown in Figure 1, high-frequency geometric details are obtained on a smooth base surface by taking samples from the base surface and offsetting them along their normal directions by a distance obtained (with interpolation) from a discrete height map. There are two critical elements that impede direct adoption for implicit shape representation. Firstly, the displacement mapping is defined discretely and only on the base surface, whereas implicit surface functions are typically defined continuously on the \mathbb{R}^3 domain. Secondly, while this definition assumes a known and fixed base surface, our goal is to learn the base surface and the displacement jointly on-the-fly.

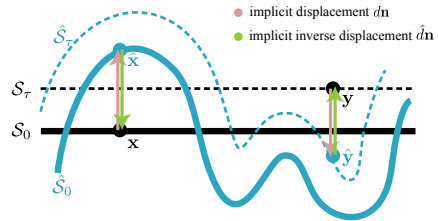


Figure 3: An implicit displacement field for a 1D-curve. The displacement is defined not only on the zero-iso-surface S_0 but also on arbitrary iso-surfaces S_τ .

Addressing the above challenges, we first define *implicit displacement fields* (IDF), which are continuous analog to height maps that extend displacement mapping to the \mathbb{R}^3 domain.

Definition 1. Given two signed distance functions f and \hat{f} and their respective iso-surfaces at a given value $\tau \in \mathbb{R}$, $S_\tau = \{\mathbf{x} \in \mathbb{R}^3 | f(\mathbf{x}) = \tau\}$ and $\hat{S}_\tau = \{\mathbf{x} \in \mathbb{R}^3 | \hat{f}(\mathbf{x}) = \tau\}$, an implicit displacement

field $d: \mathbb{R}^3 \rightarrow \mathbb{R}$ defines the deformation from \mathcal{S}_τ to $\hat{\mathcal{S}}_\tau$ such that

$$f(\mathbf{x}) = \hat{f}(\mathbf{x} + \hat{f}(\mathbf{x}) \mathbf{n}), \text{ where } \mathbf{n} = \frac{\nabla f(\mathbf{x})}{\|\nabla f(\mathbf{x})\|}. \quad (1)$$

This definition is schematically illustrated in Figure 3, where the iso-surface \mathcal{S}_0 and \mathcal{S}_τ are mapped to $\hat{\mathcal{S}}_0$ and $\hat{\mathcal{S}}_\tau$. Notably, the height map in classic displacement mapping is a discrete sampling of IDF for the limited case $\tau = 0$.

In the context of surface decomposition described in this paper, our goal is to estimate the base surface \mathcal{S}_0 and the displacement d given an explicitly represented detailed surface $\hat{\mathcal{S}}_0$. Following (1), we can learn the base SDF f and the displacement d , by minimizing the difference between the base and the ground truth signed distance at a query point \mathbf{x} and its displaced position $\hat{\mathbf{x}} = \mathbf{x} + \hat{f}(\mathbf{x}) \mathbf{n}$, *i.e.*, $\min |f(\mathbf{x}) - \hat{f}_{\text{GT}}(\hat{\mathbf{x}})|, \forall \mathbf{x} \in \mathbb{R}^3$.

However, this solution requires evaluating $\hat{f}(\hat{\mathbf{x}})$ at every iteration, which is a costly operation as the detailed shapes are typically given in explicit form, *e.g.*, as point clouds or meshes. To address this issue, we consider the inverse implicit displacement field, denoted as \hat{d} , which defines a mapping from $\hat{\mathcal{S}}_\tau$ to \mathcal{S}_τ as depicted in Figure 3:

$$f(\hat{\mathbf{x}} + \hat{d}(\hat{\mathbf{x}}) \hat{\mathbf{n}}) = \hat{f}(\hat{\mathbf{x}}). \quad (2)$$

Assuming the displacement distance is small, we can replace \mathbf{n} , the normal after inverse displacement, with that before the inverse displacement, *i.e.*

$$f(\hat{\mathbf{x}} + \hat{d}(\hat{\mathbf{x}}) \hat{\mathbf{n}}) = \hat{f}(\hat{\mathbf{x}}), \text{ where } \hat{\mathbf{n}} = \frac{\nabla f(\hat{\mathbf{x}})}{\|\nabla f(\hat{\mathbf{x}})\|}. \quad (3)$$

This is justified by the following theorem and corollary, which we prove in the Appendix A.

Theorem 1. *If function $f: \mathbb{R}^n \rightarrow \mathbb{R}$ is differentiable, Lipschitz-continuous with constant L and Lipschitz-smooth with constant M , then $\|\nabla f(\mathbf{x} + \delta \nabla f(\mathbf{x})) - \nabla f(\mathbf{x})\| \leq |\delta|LM$.*

Corollary 1. *If a signed distance function f satisfying the eikonal equation up to error $\epsilon > 0$, $|\|\nabla f\| - 1| < \epsilon$, is Lipschitz-smooth with constant M , then $\|\nabla f(\mathbf{x} + \delta \nabla f(\mathbf{x})) - \nabla f(\mathbf{x})\| < (1 + \epsilon)|\delta|M$.*

Recall that $\mathbf{n} = \frac{\nabla f(\mathbf{x})}{\|\nabla f(\mathbf{x})\|}$ and $\hat{\mathbf{x}} = \mathbf{x} + \hat{d}(\hat{\mathbf{x}}) \hat{\mathbf{n}}$, by setting $\delta = \hat{d}/\|\nabla f(\mathbf{x})\|$ we have $\|\nabla f(\mathbf{x}) - \nabla f(\hat{\mathbf{x}})\| < (1 + \epsilon)|\delta|M$, *i.e.* the difference of unnormalized normals at \mathbf{x} and $\hat{\mathbf{x}}$ is small. Using Eikonal equation, we can thus assume the difference of the normalized ones \mathbf{n} and $\hat{\mathbf{n}}$ is also small, therefore obtain (3).

The advantage of the formulation in (3) is that it allows supervision using precomputed the ground truth signed distance values, as well as any ground truth derivatives (see Section 3.2) at a set of sample locations $\hat{\mathbf{x}}$.

3.2 Network design and training

The formulation (inverse) implicit field in the previous section is based on three assumptions: (i) f must be smooth, (ii) d must be small, (iii) f must satisfy the eikonal constraint up to an error bound. In this section, we describe our network architecture and training technique, with emphasis on meeting these requirements.

Network architecture. We propose to model f and \hat{d} with two SIRENS denoted as \mathcal{N}^{ω_B} and \mathcal{N}^{ω_D} , where ω_B and ω_D refer to the frequency hyperparameter in the sine activation functions $\mathbf{x} \mapsto \sin(\omega \mathbf{x})$. Evidently, as shown in Figure 4, ω dictates an upper bound on the frequencies the network is capable of representing, thereby also determining the network’s inductive bias for smoothness. Correspondingly, we enforce the smoothness of f and detail-representing capacity of \hat{d} using a smaller ω_B and a larger ω_D . Empirically, we find that $\omega_B = 15$ and $\omega_D = 60$ fits our needs in most cases. Moreover, we add a scaled tanh activation to the last linear layer of \mathcal{N}^{ω_D} , *i.e.* $\alpha \tanh(\cdot)$, which ensures that the displacement distance is smaller than the constant α .

Networks containing high-frequency signals, *e.g.* \mathcal{N}^{ω_D} , require large amounts of accurate ground truth data for supervision to avoid running into optimization local minima [35]. Consequently, when



Figure 4: Smoothness control via SIREN’s frequency hyperparameter ω . Overfitting SIREN to the first image with $\omega = 30$ (middle) and $\omega = 60$ (right) shows that smaller ω leads to a smoother result.

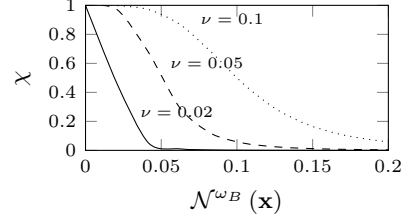


Figure 5: Attenuation as a function of base SDF.

dense and accurate ground truth SDF values are not available, high-frequency signals often create artifacts. This is often the case in void regions when learning from point clouds, as only implicit regularization and fuzzy supervision is applied (see the first and last terms of (7)). To address this issue, we apply the following attenuation function χ to subdue \mathcal{N}^{ω_D} depending on the distance to the base surface \mathcal{S}_0 :

$$\chi(\mathcal{N}^{\omega_B}) = \frac{1}{1 + (\mathcal{N}^{\omega_B}(\mathbf{x})/\nu)^4}, \quad (4)$$

where ν determines the speed of attenuation, as shown in Figure 5.

Combining the aforementioned components, we can compute the signed distance of the detailed shape at query point \mathbf{x} in two steps:

$$f(\mathbf{x}) = \mathcal{N}^{\omega_B}(\mathbf{x}) \quad (5)$$

$$\hat{f}(\mathbf{x}) = \mathcal{N}^{\omega_B} \left(\mathbf{x} + \chi(f(\mathbf{x})) \mathcal{N}^{\omega_D}(\mathbf{x}) \frac{\nabla f(\mathbf{x})}{\|\nabla f(\mathbf{x})\|} \right). \quad (6)$$

Training. Our implicit displacement formulated in (3) allows us to train the networks without ground truth signed distance values. Thus we adopt the loss from SIREN, which is constructed to learn SDFs directly from oriented point clouds by solving the eikonal equation with boundary constraint at the on-surface points. Denoting the input domain as Ω (by default set to $[-1, 1]^3$) and the ground truth point cloud as $\mathcal{P} = \{(\mathbf{p}_i, \mathbf{n}_i)\}$, the loss is

$$\begin{aligned} \mathcal{L}_{\hat{f}} = & \sum_{\mathbf{x} \in \Omega} \lambda_0 \left| \|\nabla \hat{f}(\mathbf{x})\| - 1 \right| + \sum_{(\mathbf{p}, \mathbf{n}) \in \mathcal{P}} \left(\lambda_1 |\hat{f}(\mathbf{p})| + \lambda_2 \left(1 - \langle \nabla \hat{f}(\mathbf{p}), \mathbf{n} \rangle \right) \right) \\ & + \sum_{\mathbf{x} \in \Omega \setminus \mathcal{P}} \lambda_3 \exp \left(-100 \hat{f}(\mathbf{x}) \right), \end{aligned} \quad (7)$$

where $\lambda_{\{0,1,2,3\}}$ denote loss weights.

As the displacement and the attenuation functions depend on the base network, it is beneficial to have a well-behaving base network when training the displacement (see Section 4.2). Therefore, we adopt a progressive learning scheme, which first trains \mathcal{N}^{ω_B} , and then gradually increase the impact of \mathcal{N}^{ω_D} . Notably, this frequency-based coarse-to-fine training technique has been adopted in recent works [35, 25], where it contributed to better optimization results.

We implement the progressive training via symmetrically diminishing/increasing learning rates and loss weights for the base/displacement networks. For brevity, we describe the procedure for loss weights only, and we apply the same to the learning rates in our implementation. First, we train \mathcal{N}^{ω_B} by substituting \hat{f} in the loss (7) with f , resulting a base-only loss denoted \mathcal{L}_f . Then, starting from a training percentile $T_m \in [0, 1]$, we combine \mathcal{L}_f and $\mathcal{L}_{\hat{f}}$ via

$$\kappa \mathcal{L}_f + (1 - \kappa) \mathcal{L}_{\hat{f}} \quad \text{with} \quad \kappa = \frac{1}{2} \left(1 + \cos \left(\pi \frac{(t - T_m)}{(1 - T_m)} \right) \right), \quad (8)$$

where $t \in [T_m, 1]$ denotes the current training progress.

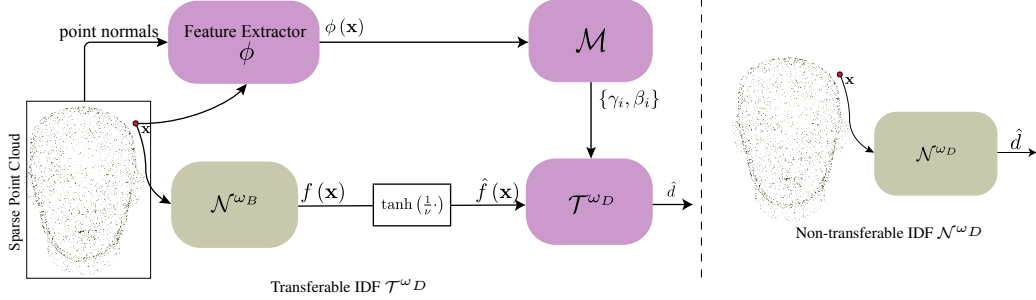


Figure 6: Illustrations for transferable and non-transferable implicit fields. The transferable modules are in pink and the shape-specific modules are in yellow.

3.3 Transferable implicit displacement field.

As mentioned earlier, one advantage of using classic displacement mapping to create surface details is that once the mapping, known as surface parameterization, from the base surface to the height map is created, the displacement is independent of deformations of the base surface. We aim to emulate this effect for IDF by extending classical UV-coordinates produced by a surface parameterization to \mathbb{R}^3 . While there are many ways to achieve this goal, in this paper we are interested in learning such extended coordinates, referred to as *query features*, from a single source shape without surface parameterization or correspondence estimation. In particular, in order to train \mathcal{N}^{ω_D} with derivatives as in (7), the query features must be differentiable with respect to the coordinates of the query point.

We construct the query features using two pieces of information: (i) a global context descriptor, $\phi(\mathbf{x})$, describing the location of the query point in relation to the base surface in a semantically meaningful way, (ii) the base signed distance value $f(\mathbf{x})$, which gives more precise relative location with respect to the base surface. In the following, we first describe the global context descriptor and then introduce the necessary modifications to \mathcal{N}^{ω_D} so as to effectively learn from the combined information.

There exist many point feature extractors, mostly notably [39, 40], but none of them can produce features for off-surface points. Inspired by occupancy convolutional networks (OCN) [36], we project the sparse on-surface point features obtained using a conventional point cloud encoder on a regular 3D (or 2D, *c.f.* Section 4.3) grid, which is then fed to a convolutional module to propagate sparse on-surface point features to the off-surface area; finally, the query feature is obtained from the feature grids using bilinear interpolation. In our implementation, since our entire training data is a single shape, we reduce the depth of the point cloud encoder by half to mitigate the risk of overfitting. Furthermore, we use normals instead of point positions as the input to the point cloud encoder, making the features scale-invariant and translation-invariant. Note that ideally the features should also be rotation-invariant. Nevertheless, as we empirically show later, normal features can in fact generalize under small local rotational deformations, which is sufficient for transferring displacements between two roughly aligned shapes. We leave further explorations in this direction for future work.

Now \mathcal{N}^{ω_D} is tasked to predict the displacement value conditioning on $\phi(\mathbf{x})$ and $f(\mathbf{x})$. However, our empirical results suggest that SIREN does not handle high-dimensional inputs well (in our case, a 17-D vector, with $\phi(\mathbf{x})$ being 16-D). Therefore we adopt the FiLM conditioning [37, 19] as suggested by Pi-GAN [9], which feeds the conditioning latent vector not as part of the network input but rather as an affine transformation to the features of each layer. Specifically, treating $\phi(\mathbf{x})$ as the conditioning latent vector, a mapping network \mathcal{M} maps $\phi(\mathbf{x})$ to a set of C-dimensional frequency modulators and phase shifters $\{\gamma_i, \beta_i\}$, which are used to transform the i -th MLP layers to

$$\left(\mathbf{1} + \frac{1}{2} \gamma_i \right) \circ (\mathbf{W}_i \mathbf{x} + \mathbf{b}_i) + \beta_i, \quad (9)$$

where \mathbf{W}_i and \mathbf{b}_i are the trainable parameters in the MLP layer and \circ denotes element-wise multiplication.

Since SIREN assumes normalized inputs in range $(-1, 1)$ and the base signed distance value $f(\mathbf{x})$ is small close to the \mathcal{S}_0 surface, where the displacement really matters, we scale $f(\mathbf{x})$ with the following function before feeding it to the FiLM SIREN network:

$$\bar{f}(\mathbf{x}) = \tanh\left(\frac{1}{\nu} f(\mathbf{x})\right), \quad (10)$$

	Chamfer distance points to point distance $\cdot 10^{-3}$ / normal cosine distance $\cdot 10^{-2}$							
	Progressive FFN	NGLOD (LOD4)	NGLOD (LOD6)	SIREN-3 $\omega = 60$	SIREN-7 $\omega = 30$	SIREN-7 $\omega = 60$	Direct Residual	Ours
asian dragon	4.96 / 4.02	1.66 / 4.05	1.03 / 1.91	6.13 / 5.28	3.65 / 2.36	7.24 / 4.03	17.3 / 18.9	0.94 / 1.36
camera	4.62 / 1.51	1.56 / 1.15	1.32 / 0.62	6.49 / 2.38	4.11 / 1.10	-	49.7 / 38.5	1.29 / 0.34
dragon	5.10 / 4.00	1.80 / 3.77	1.39 / 2.37	7.04 / 4.75	3.80 / 2.49	-	81.3 / 19.5	1.27 / 1.50
warrior	5.94 / 7.25	2.46 / 8.12	1.52 / 5.21	7.27 / 8.45	3.68 / 4.83	5.96 / 8.01	-	1.49 / 4.56
dragon wing	5.68 / 5.41	2.01 / 4.98	1.47 / 2.87	6.57 / 5.46	7.92 / 3.84	-	-	1.35 / 1.49
ramesses	4.24 / 2.30	1.47 / 2.47	0.97 / 1.93	6.40 / 3.77	4.20 / 2.33	-	-	1.35 / 1.58
thai statue	5.23 / 7.01	7.16 / 16.7	1.30 / 4.77	6.26 / 7.48	3.81 / 4.17	-	-	0.92 / 2.92
vase lion	5.92 / 1.93	1.86 / 2.18	1.39 / 0.77	39.8 / 25.6	4.68 / 1.02	-	87.0 / 30.7	1.33 / 0.42
average	5.21 / 4.18	2.50 / 5.43	1.30 / 2.56	10.8 / 7.90	4.48 / 2.77	-	-	1.24 / 1.77

Table 1: Extended quantitative comparison. Among the benchmarking methods, only NGLOD at LOD-6, using $256 \times$ number of parameters compared to our model, can yield results close to ours. SIREN models with larger ω have severe convergence issues: despite our best efforts, the models still diverged in a majority of cases (see Figure 8 for examples). Similarly Direct Residual using $\omega = 60$ in the displacement net suffers from the same convergence issue.

where ν is the attenuation parameter in (4).

Denoting the modified displacement network as \mathcal{T}^{ω_D} , we illustratively summarize the difference between transferable and non-transferable displacement field in Figure 6. In summary, the signed distance function of the detailed shape in (6) can be rewritten as

$$\hat{f}(\mathbf{x}) = \mathcal{N}^{\omega_B} \left(\mathbf{x} + \chi(f(\mathbf{x})) \mathcal{T}^{\omega_D}(\bar{f}(\mathbf{x}), \mathcal{M}(\phi(\mathbf{x}))) \frac{\nabla f(\mathbf{x})}{\|\nabla f(\mathbf{x})\|} \right). \quad (11)$$

4 Results

We now present the results of our method. Additional results can be found in the supplemental material. In Section 4.1, we evaluate our networks in terms of geometric detail representation by comparing with state-of-the-art methods on the single shape fitting task. We then evaluate various design components in an ablation study in Section 4.2. Finally, we validate the transferability of the displacement fields in a detail transfer task in Section 4.3.

Implementation details. Except in Section 4.3, we use $\omega_B = 15$ and $\omega_D = 60$. By default, both the base and the displacement nets have 4 hidden layers with 256 channels each. The maximal displacement and attenuation factors described in Section 3.2 are set to $\alpha = 0.05$ and $\nu = 0.02$. The loss weights $\lambda_{\{0,1,2,3\}}$ in (7) are set to 5, 400, 40 and 50, respectively, and the switching training percentile in (8) is set to $T_m = 0.2$. We train our models for 120 epochs using batch size 5000 and ADAM optimizer with initial learning rate of 0.0001, then gradually reduce the learning rate to 0.00001 using cosine annealing [29] after finishing 80% of the training epochs. Furthermore, to improve the convergence rate, we initialize SIREN models by pre-training the base model \mathcal{N}^{ω_B} (and baseline SIREN, *c.f.* Section 4.1) to a sphere with radius 0.5. This initialization is optional for our training but is critical for baseline SIREN’s convergence.

Data. We test our method using 8 high-resolution shapes, including 6 from Sketchfab [1] under CC-BY-4.0 and 2 from Stanford 3DScanRepo [2]. Our transferable displacement model is tested using the FaceScape dataset [53]. We obtain the high-resolution mesh by first filling the holes in the provided low-resolution meshes using [3] and then applying the 4K displacement maps provided by the original dataset. We also use meshes provided by Berkiten et al. [5], which contains pairs of already separated base and detailed shapes.

4.1 Detail representation.

The methods we compare with are 1) Fourier feature network [51] with SOFTPLUS activation and 8 frequency bands trained from coarse-to-fine, as suggested by Park et al. [35]; a total of 8 hidden layers each of size 256 are used to match our model size; additionally we apply a skip-connection in the middle layer as proposed in DeepSDF Park et al. [34]; 2) NGLOD [50] trained using 4 and 6 levels of detail (LODs) corresponding to 64^3 and 256^3 spatial resolution respectively, with LOD4 comparable with our model in terms of the number of parameters, 3) baseline SIREN, for which we

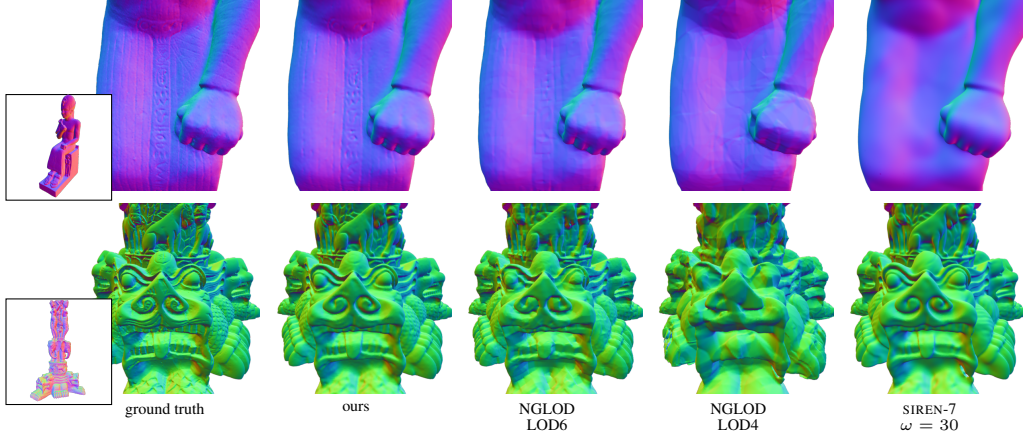


Figure 7: Comparison of detail reconstruction (better viewed with zoom-in). We show the best 4 methods according to Table 1, more results are provided in the supplemental.

trained three different variations in hope of overcoming training divergence issues; 4) direct residual, where we compose the signed distance value simply as the sum of base and displacement nets. *i.e.* $\hat{f}(\mathbf{x}) = \mathcal{N}^{\omega_B}(\mathbf{x}) + \mathcal{N}^{\omega_D}(\mathbf{x})$. Since NGLOD requires ground truth SDF for supervision, we train it using the original implementation, for the rest methods we follow the same training protocol whenever possible and report the best result we can obtain. Two-way point-to-point distance and normal cosine distance are computed as the evaluation metrics on 5 million points randomly sampled from meshes extracted using marching cubes with 512^3 resolution.

As shown in Table 1, NGLOD trained with 6 LODs is the only method comparable with ours in terms of reconstruction accuracy. Relying on spatial partition, NGLOD LOD6 requires storing more than 300 times as many as parameters as our model, yet as Figure 7 shows, our model represents the detailed geometries with much higher fidelity and overwhelmingly outperforms LOD4, which is still around 3 times as large as our model. SIREN networks with larger ω have severe convergence issues. In order to match our model size and frequency, we attempted training with 7 hidden layers and $\omega = 60$ (SIREN-7 $\omega = 60$), but the training fails for most shapes even with sphere initialization (*c.f.* Implementation Details) and gradient clipping, as shown in Figure 8. Direct residual differs from our method in that the displacement network simply predicts a residual signed distance value for the base network, and consequently the displacement net does not depend on the base surface by construction, which leads to similar convergence issues as baseline SIRENs with large ω .

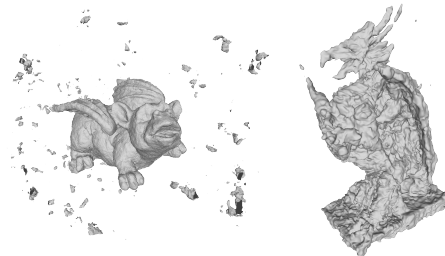


Figure 8: Example results from diverged SIREN and Direct Residual training.

4.2 Ablation study

We study the effect of different design components described in Section 3.2, including the displacement scaling $\alpha \tanh$, the attenuation function χ and the progressive training (7). First, as Table 2 shows, all the test modes converge within comparable range, even for the model with the least constraints. This shows that our model is robust against violations of theoretical assumptions specified in Section 3.1. At the same time, the performance rises with increasingly constrained architecture and progressive training, suggesting that the proposed mechanisms further boost training stability.

$\alpha \tanh$	χ	prog. training	average CD $\cdot 10^{-3}$
			1.44
✓			1.41
✓	✓		1.38
✓	✓	✓	1.24

Table 2: Ablation study. Our model benefits from the proposed architectural and training designs, yet it is also robust against variations.

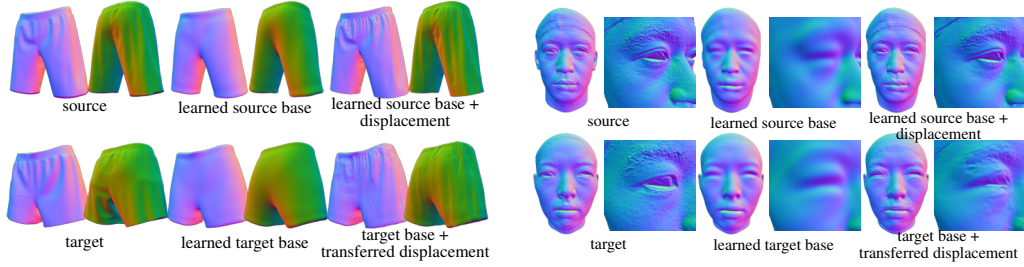


Figure 10: Transferable IDF applied to detail transfer.

4.3 Transferability

We apply our method to detail transfer in order to validate the transferability of IDF. Specifically, we want to transfer the displacements learned for a source shape to an aligned but different target shape. In the first test scenario, the base shape is provided and lies closely to the ground truth detailed surface. In the second scenario, we are only provided with the detailed shapes and thus need to estimate the base and the displacements jointly. The pipeline consists of the following steps: 1) training \mathcal{N}^{ω_B} by fitting the source shape (or the source base shape if provided), 2) training \mathcal{T}^{ω_D} , \mathcal{M} and the query feature extractor ϕ jointly by fitting the source shape using (11) while keeping \mathcal{N}^{ω_B} fixed, 3) training $\mathcal{N}_{new}^{\omega_B}$ by fitting the target shape (or the target base shape if provided), 4) evaluating (11) by replacing \mathcal{N}^{ω_B} with $\mathcal{N}_{new}^{\omega_B}$. In our experiment, we subsample 3000 oriented points as the input to the feature extractor. To prevent the base network from learning high-frequency details, we use $\omega_B = 8$ and 3 hidden layers with 96 channels each. Note that fixing \mathcal{N}^{ω_B} ensures that consistent \bar{f}_x is fed to \mathcal{T}^{ω_D} in the second training phase; in the opposite scenario where \bar{f}_x varies during training, \mathcal{T}^{ω_D} tends to ignore this input and consequently overfits to $\phi(x)$.

Example outputs for both scenarios are shown in Figure 10; the base shapes are provided for the *shorts* model. We use a 32^3 and a 128^2 grid (for the frontal view), for the *shorts* and *face* model respectively in our modified OCN to extract the query features. Our displacement fields, learned solely from the source shape, generate plausible details on the unseen target shape. The transferred details contain high-frequency signals (e.g. the eyebrows on the face), which is challenging for explicit representations. However, for the second scenario the performance degenerates slightly since the displacement field has to compensate errors stemming specifically from the base SDF. Notably, scaling the base signed distance value before feeding it to \mathcal{T}^{ω_D} is critical to avoid artifacts at the boundary (as shown on the Figure 9).



Figure 9: Detail transfer without scaling in (10).

5 Conclusion and limitations

In this paper, we proposed a new parameterization of neural implicit functions for detailed geometry representation. Extending displacement mapping, a classic shape modeling technique, our formulation represents a given shape by a smooth base surface and a high-frequency displacement field that offsets the base surface along its normal directions. This resulting frequency partition enables the network to concentrate on regions with rich geometric details, significantly boosting its representational power. Thanks to the theoretically grounded network design, the high-frequency signal is well constrained, and as a result our model shows convergence qualities compared to other models leveraging high-frequency signals, such as SIREN and positional encoding. Furthermore, emulating the deformation-invariant quality of classic displacement mapping, we extend our method to enable transferability of the implicit displacements, thus making it possible to use implicit representations for new geometric modeling tasks.

A limitation of our detail transfer application is the necessity to pre-align the two shapes. In future work, we consider exploring sparse correspondences as part of the input, which is a common practice in computer graphics applications, to facilitate subsequent automatic shape alignment.

Acknowledgments and Disclosure of Funding

This work is sponsored by Apple’s AI/ML PhD fellowship program.

References

- [1] Sketchfab. <https://sketchfab.com>, 2021.
- [2] Stanford 3d scan repository. <http://graphics.stanford.edu/data/3Dscanrep/>, 2021.
- [3] Marco Attene. A lightweight approach to repairing digitized polygon meshes. *The visual computer*, 26(11):1393–1406, 2010.
- [4] Ronen Basri, Meirav Galun, Amnon Geifman, David Jacobs, Yoni Kasten, and Shira Kritchman. Frequency bias in neural networks for input of non-uniform density. In *International Conference on Machine Learning*, pages 685–694. PMLR, 2020.
- [5] Sema Berkiten, Maciej Halber, Justin Solomon, Chongyang Ma, Hao Li, and Szymon Rusinkiewicz. Learning detail transfer based on geometric features. *Computer Graphics Forum*, 36(2):361–373, 2017.
- [6] Henning Biermann, Ioana Martin, Fausto Bernardini, and Denis Zorin. Cut-and-paste editing of multiresolution surfaces. *ACM Transactions on Graphics (TOG)*, 21(3):312–321, 2002.
- [7] Mario Botsch, Leif Kobbelt, Mark Pauly, Pierre Alliez, and Bruno Lévy. *Polygon mesh processing*. CRC press, 2010.
- [8] Rohan Chabra, Jan E Lenssen, Eddy Ilg, Tanner Schmidt, Julian Straub, Steven Lovegrove, and Richard Newcombe. Deep local shapes: Learning local sdf priors for detailed 3d reconstruction. In *European Conference on Computer Vision*, pages 608–625. Springer, Springer International Publishing, 2020.
- [9] Eric R Chan, Marco Monteiro, Petr Kellnhofer, Jiajun Wu, and Gordon Wetzstein. pi-gan: Periodic implicit generative adversarial networks for 3d-aware image synthesis. *arXiv preprint arXiv:2012.00926*, 2020.
- [10] Xiaobai Chen, Tom Funkhouser, Dan B Goldman, and Eli Shechtman. Non-parametric texture transfer using meshmatch. *Technical Report Technical Report 2012-2*, 2012.
- [11] Yinbo Chen, Sifei Liu, and Xiaolong Wang. Learning continuous image representation with local implicit image function. *arXiv preprint arXiv:2012.09161*, 2020.
- [12] Zhiqin Chen and Hao Zhang. Learning implicit fields for generative shape modeling. In *Proceedings of the IEEE/CVF Conference on Computer Vision and Pattern Recognition*, pages 5939–5948, 2019.
- [13] Zhiqin Chen, Andrea Tagliasacchi, and Hao Zhang. Bsp-net: Generating compact meshes via binary space partitioning. In *Proceedings of the IEEE/CVF Conference on Computer Vision and Pattern Recognition*, pages 45–54, 2020.
- [14] Zhiqin Chen, Vladimir Kim, Matthew Fisher, Noam Aigerman, Hao Zhang, and Siddhartha Chaudhuri. DecorGAN: 3d shape detailization by conditional refinement. In *Proceedings of the IEEE/CVF Conference on Computer Vision and Pattern Recognition*, 2021.
- [15] Robert L Cook. Shade trees. In *Proceedings of the 11th annual conference on Computer graphics and interactive techniques*, pages 223–231, 1984.
- [16] Robert L Cook, Loren Carpenter, and Edwin Catmull. The reyes image rendering architecture. *ACM SIGGRAPH Computer Graphics*, 21(4):95–102, 1987.
- [17] Boyang Deng, John P Lewis, Timothy Jeruzalski, Gerard Pons-Moll, Geoffrey Hinton, Mohammad Norouzi, and Andrea Tagliasacchi. Nasa: neural articulated shape approximation. *arXiv preprint arXiv:1912.03207*, 2019.
- [18] Boyang Deng, Kyle Genova, Soroosh Yazdani, Sofien Bouaziz, Geoffrey Hinton, and Andrea Tagliasacchi. Cvxnet: Learnable convex decomposition. In *Proceedings of the IEEE/CVF Conference on Computer Vision and Pattern Recognition*, pages 31–44, 2020.
- [19] Vincent Dumoulin, Ethan Perez, Nathan Schucher, Florian Strub, Harm de Vries, Aaron Courville, and Yoshua Bengio. Feature-wise transformations. *Distill*, 3(7):e11, 2018.

- [20] Sarah F Frisken, Ronald N Perry, Alyn P Rockwood, and Thouis R Jones. Adaptively sampled distance fields: A general representation of shape for computer graphics. In *Proceedings of the 27th annual conference on Computer graphics and interactive techniques*, pages 249–254, 2000.
- [21] Kyle Genova, Forrester Cole, Daniel Vlasic, Aaron Sarna, William T Freeman, and Thomas Funkhouser. Learning shape templates with structured implicit functions. In *Proceedings of the IEEE/CVF International Conference on Computer Vision*, pages 7154–7164, 2019.
- [22] Kyle Genova, Forrester Cole, Avneesh Sud, Aaron Sarna, and Thomas Funkhouser. Local deep implicit functions for 3d shape. In *Proceedings of the IEEE/CVF Conference on Computer Vision and Pattern Recognition*, pages 4857–4866, 2020.
- [23] Zekun Hao, Hadar Averbuch-Elor, Noah Snively, and Serge Belongie. Dualsdf: Semantic shape manipulation using a two-level representation. In *Proceedings of the IEEE/CVF Conference on Computer Vision and Pattern Recognition*, pages 7631–7641, 2020.
- [24] Amir Hertz, Rana Hanocka, Raja Giryes, and Daniel Cohen-Or. Deep geometric texture synthesis. *ACM Trans. Graph.*, 39(4), July 2020. ISSN 0730-0301. doi: 10.1145/3386569.3392471. URL <https://doi.org/10.1145/3386569.3392471>.
- [25] Amir Hertz, Or Perel, Raja Giryes, Olga Sorkine-Hornung, and Daniel Cohen-Or. Progressive encoding for neural optimization. *arXiv preprint arXiv:2104.09125*, 2021.
- [26] Chiyu Jiang, Avneesh Sud, Ameesh Makadia, Jingwei Huang, Matthias Nießner, Thomas Funkhouser, et al. Local implicit grid representations for 3d scenes. In *Proceedings of the IEEE/CVF Conference on Computer Vision and Pattern Recognition*, pages 6001–6010, 2020.
- [27] Manyi Li and Hao Zhang. D²im-net: Learning detail disentangled implicit fields from single images. In *Proceedings of the IEEE/CVF Conference on Computer Vision and Pattern Recognition*, 2021.
- [28] Lingjie Liu, Jiatao Gu, Kyaw Zaw Lin, Tat-Seng Chua, and Christian Theobalt. Neural sparse voxel fields. In H. Larochelle, M. Ranzato, R. Hadsell, M. F. Balcan, and H. Lin, editors, *Advances in Neural Information Processing Systems*, volume 33, pages 15651–15663. Curran Associates, Inc., 2020. URL <https://proceedings.neurips.cc/paper/2020/file/b4b758962f17808746e9bb832a6fa4b8-Paper.pdf>.
- [29] Ilya Loshchilov and Frank Hutter. Sgdr: Stochastic gradient descent with warm restarts. *arXiv preprint arXiv:1608.03983*, 2016.
- [30] Lars Mescheder, Michael Oechsle, Michael Niemeyer, Sebastian Nowozin, and Andreas Geiger. Occupancy networks: Learning 3d reconstruction in function space. In *Proceedings of the IEEE/CVF Conference on Computer Vision and Pattern Recognition*, pages 4460–4470, 2019.
- [31] Ben Mildenhall, Pratul P Srinivasan, Matthew Tancik, Jonathan T Barron, Ravi Ramamoorthi, and Ren Ng. Nerf: Representing scenes as neural radiance fields for view synthesis. In *European Conference on Computer Vision*, pages 405–421. Springer, Springer International Publishing, 2020.
- [32] Michael Niemeyer, Lars Mescheder, Michael Oechsle, and Andreas Geiger. Differentiable volumetric rendering: Learning implicit 3d representations without 3d supervision. In *Proceedings of the IEEE/CVF Conference on Computer Vision and Pattern Recognition*, pages 3504–3515, 2020.
- [33] Yutaka Ohtake, Alexander Belyaev, Marc Alexa, Greg Turk, and Hans-Peter Seidel. Multi-level partition of unity implicits. *ACM Trans. Graph.*, 22(3):463–470, 2003. ISSN 0730-0301. doi: 10.1145/882262.882293. URL <https://doi.org/10.1145/882262.882293>.
- [34] Jeong Joon Park, Peter Florence, Julian Straub, Richard Newcombe, and Steven Lovegrove. DeepSDF: Learning continuous signed distance functions for shape representation. In *Proceedings of the IEEE/CVF Conference on Computer Vision and Pattern Recognition*, pages 165–174, 2019.
- [35] Keunhong Park, Utkarsh Sinha, Jonathan T. Barron, Sofien Bouaziz, Dan B Goldman, Steven M. Seitz, and Ricardo Martin-Brualla. Deformable neural radiance fields. *arXiv preprint arXiv:2011.12948*, 2020.
- [36] Songyou Peng, Michael Niemeyer, Lars Mescheder, Marc Pollefeys, and Andreas Geiger. Convolutional occupancy networks. In *European Conference on Computer Vision (ECCV)*, Cham, August 2020. Springer International Publishing.
- [37] Ethan Perez, Florian Strub, Harm De Vries, Vincent Dumoulin, and Aaron Courville. Film: Visual reasoning with a general conditioning layer. In *Proceedings of the AAAI Conference on Artificial Intelligence*, 2018.

- [38] Albert Pumarola, Enric Corona, Gerard Pons-Moll, and Francesc Moreno-Noguer. D-nerf: Neural radiance fields for dynamic scenes. *arXiv preprint arXiv:2011.13961*, 2020.
- [39] Charles R Qi, Hao Su, Kaichun Mo, and Leonidas J Guibas. Pointnet: Deep learning on point sets for 3d classification and segmentation. In *Proceedings of the IEEE conference on computer vision and pattern recognition*, pages 652–660, 2017.
- [40] Charles R Qi, Li Yi, Hao Su, and Leonidas J Guibas. Pointnet++: Deep hierarchical feature learning on point sets in a metric space. *arXiv preprint arXiv:1706.02413*, 2017.
- [41] Nasim Rahaman, Aristide Baratin, Devansh Arpit, Felix Draxler, Min Lin, Fred Hamprecht, Yoshua Bengio, and Aaron Courville. On the spectral bias of neural networks. In *International Conference on Machine Learning*, pages 5301–5310. PMLR, 2019.
- [42] Shunsuke Saito, Zeng Huang, Ryota Natsume, Shigeo Morishima, Angjoo Kanazawa, and Hao Li. Pifu: Pixel-aligned implicit function for high-resolution clothed human digitization. In *Proceedings of the IEEE/CVF International Conference on Computer Vision*, pages 2304–2314, 2019.
- [43] Shunsuke Saito, Tomas Simon, Jason Saragih, and Hanbyul Joo. Pifuhd: Multi-level pixel-aligned implicit function for high-resolution 3d human digitization. In *Proceedings of the IEEE/CVF Conference on Computer Vision and Pattern Recognition*, pages 84–93, 2020.
- [44] Vincent Sitzmann, Michael Zollhöfer, and Gordon Wetzstein. Scene representation networks: Continuous 3d-structure-aware neural scene representations. *arXiv preprint arXiv:1906.01618*, 2019.
- [45] Vincent Sitzmann, Julien Martel, Alexander Bergman, David Lindell, and Gordon Wetzstein. Implicit neural representations with periodic activation functions. In H. Larochelle, M. Ranzato, R. Hadsell, M. F. Balcan, and H. Lin, editors, *Advances in Neural Information Processing Systems*, volume 33, pages 7462–7473. Curran Associates, Inc., 2020. URL <https://proceedings.neurips.cc/paper/2020/file/53c04118df112c13a8c34b38343b9c10-Paper.pdf>.
- [46] Ivan Skorokhodov, Savva Ignatyev, and Mohamed Elhoseiny. Adversarial generation of continuous images. *arXiv preprint arXiv:2011.12026*, 2020.
- [47] Olga Sorkine and Mario Botsch. Tutorial: Interactive shape modeling and deformation. In *EUROGRAPHICS*, 2009.
- [48] Olga Sorkine, Daniel Cohen-Or, Yaron Lipman, Marc Alexa, Christian Rössl, and H-P Seidel. Laplacian surface editing. In *Proceedings of the 2004 Eurographics/ACM SIGGRAPH symposium on Geometry processing*, pages 175–184, 2004.
- [49] Kenshi Takayama, Ryan Schmidt, Karan Singh, Takeo Igarashi, Tamy Boubekeur, and Olga Sorkine. Geobrush: Interactive mesh geometry cloning. *Computer Graphics Forum*, 30(2):613–622, 2011.
- [50] Towaki Takikawa, Joey Litalien, Kangxue Yin, Karsten Kreis, Charles Loop, Derek Nowrouzezahrai, Alec Jacobson, Morgan McGuire, and Sanja Fidler. Neural geometric level of detail: Real-time rendering with implicit 3D shapes. In *Proceedings of the IEEE/CVF Conference on Computer Vision and Pattern Recognition*, 2021.
- [51] Matthew Tancik, Pratul Srinivasan, Ben Mildenhall, Sara Fridovich-Keil, Nithin Raghavan, Utkarsh Singhal, Ravi Ramamoorthi, Jonathan Barron, and Ren Ng. Fourier features let networks learn high frequency functions in low dimensional domains. In H. Larochelle, M. Ranzato, R. Hadsell, M. F. Balcan, and H. Lin, editors, *Advances in Neural Information Processing Systems*, volume 33, pages 7537–7547. Curran Associates, Inc., 2020. URL <https://proceedings.neurips.cc/paper/2020/file/55053683268957697aa39fba6f231c68-Paper.pdf>.
- [52] Edgar Tretschk, Ayush Tewari, Vladislav Golyanik, Michael Zollhöfer, Carsten Stoll, and Christian Theobalt. Patchnets: Patch-based generalizable deep implicit 3d shape representations. In *European Conference on Computer Vision*, pages 293–309. Springer, Springer International Publishing, 2020.
- [53] Haotian Yang, Hao Zhu, Yanru Wang, Mingkai Huang, Qiu Shen, Ruigang Yang, and Xun Cao. Facescape: a large-scale high quality 3d face dataset and detailed riggable 3d face prediction. In *Proceedings of the IEEE Conference on Computer Vision and Pattern Recognition (CVPR)*, 2020.
- [54] Lior Yariv, Yoni Kasten, Dror Moran, Meirav Galun, Matan Atzmon, Basri Ronen, and Yaron Lipman. Multiview neural surface reconstruction by disentangling geometry and appearance. *Advances in Neural Information Processing Systems*, 33, 2020.

- [55] Wang Yifan, Noam Aigerman, Vladimir G Kim, Siddhartha Chaudhuri, and Olga Sorkine-Hornung. Neural cages for detail-preserving 3d deformations. In *Proceedings of the IEEE/CVF Conference on Computer Vision and Pattern Recognition*, pages 75–83, 2020.
- [56] Lexing Ying, Aaron Hertzmann, Henning Biermann, and Denis Zorin. Texture and shape synthesis on surfaces. In *Eurographics Workshop on Rendering Techniques*, pages 301–312. Springer, 2001.
- [57] Howard Zhou, Jie Sun, Greg Turk, and James M Rehg. Terrain synthesis from digital elevation models. *IEEE transactions on visualization and computer graphics*, 13(4):834–848, 2007.
- [58] Kun Zhou, Xin Huang, Xi Wang, Yiying Tong, Mathieu Desbrun, Baining Guo, and Heung-Yeung Shum. Mesh quilting for geometric texture synthesis. In *ACM SIGGRAPH 2006 Papers*, pages 690–697. 2006.

A Proof

Theorem 1. *If function $f : \mathbb{R}^n \rightarrow \mathbb{R}$ is differentiable, Lipschitz-continuous with constant L and Lipschitz-smooth with constant M , then $\|\nabla f(\mathbf{x} + \delta \nabla f(\mathbf{x})) - \nabla f(\mathbf{x})\| \leq |\delta|LM$.*

Proof. If a differentiable function f is Lipschitz-continuous with constant L and Lipschitz-smooth with constant M , then

$$\|\nabla f(\mathbf{x})\| \leq L \tag{12}$$

$$\|\nabla f(\mathbf{x}) - \nabla f(\mathbf{y})\| \leq M\|\mathbf{x} - \mathbf{y}\|. \tag{13}$$

$$\begin{aligned} \|\nabla f(\mathbf{x} + \delta \nabla f(\mathbf{x})) - \nabla f(\mathbf{x})\| &\leq M\|\delta \nabla f(\mathbf{x})\| && \text{by (13)} \\ &\leq |\delta|LM && \text{by (12)} \end{aligned}$$

□

Corollary 1. *If a signed distance function f satisfying the eikonal equation up to error $\epsilon > 0$, $\left| \|\nabla f\| - 1 \right| < \epsilon$, is Lipschitz-smooth with constant M , then $\|\nabla f(\mathbf{x} + \delta \nabla f(\mathbf{x})) - \nabla f(\mathbf{x})\| < (1 + \epsilon)|\delta|M$.*

Proof. $\left| \|\nabla f\| - 1 \right| < \epsilon \Leftrightarrow \|\nabla f\| < \epsilon + 1$. This means f is Lipschitz-continuous with constant $\epsilon + 1$. Then by Theorem 1, $\|\nabla f(\mathbf{x} + \delta \nabla f(\mathbf{x})) - \nabla f(\mathbf{x})\| < |\delta|(1 + \epsilon)M$.

□

B Multi-target detail transfer

Once trained, ϕ and \mathcal{T}^{ω_D} can be deployed to a new base surface without any fine-tuning or adaptation. In other words, given a target shape, we only need to fit a new base network $\mathcal{N}_{\text{new}}^{\omega_B}$, then compute the inverse displacement \hat{d} and the composed SDF $\hat{f}(\mathbf{x})$ simply by replacing replacing \mathcal{N}^{ω_B} with $\mathcal{N}_{\text{new}}^{\omega_B}$. We show the result of this process in Figure 11. It is worth mentioning that even though the point extractor is trained on a single source shape, it is able to generalize across different identities thanks to the built-in scale and translation invariance.

C Detail representation

We provide visual comparison for the tested models and methods in Figure 12.

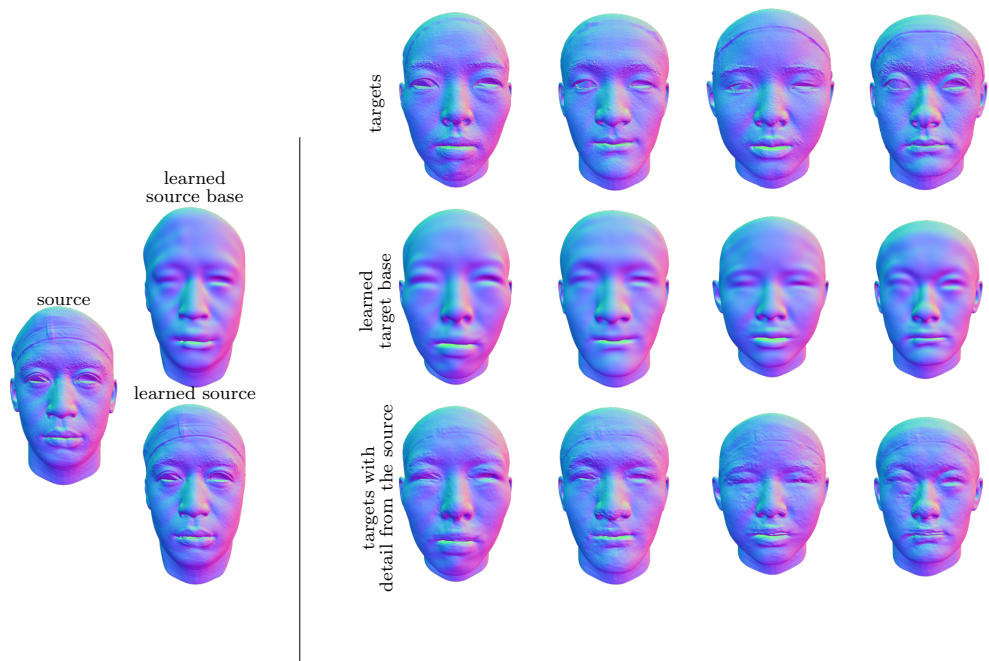


Figure 11: Detail transfer to multiple similarly aligned target shapes. Given a (detailed) source shape, we train a base network \mathcal{N}^{ω_B} to represent the smooth base surface (see *learned source base*), as well as a feature extractor ϕ and a transferrable displacement network \mathcal{T}^{ω_D} to represent the surface details. During detail transfer, we only need to fit the lightweight base network for each new target, while the feature extractor and displacement net can be applied to the new shapes without adaptation.

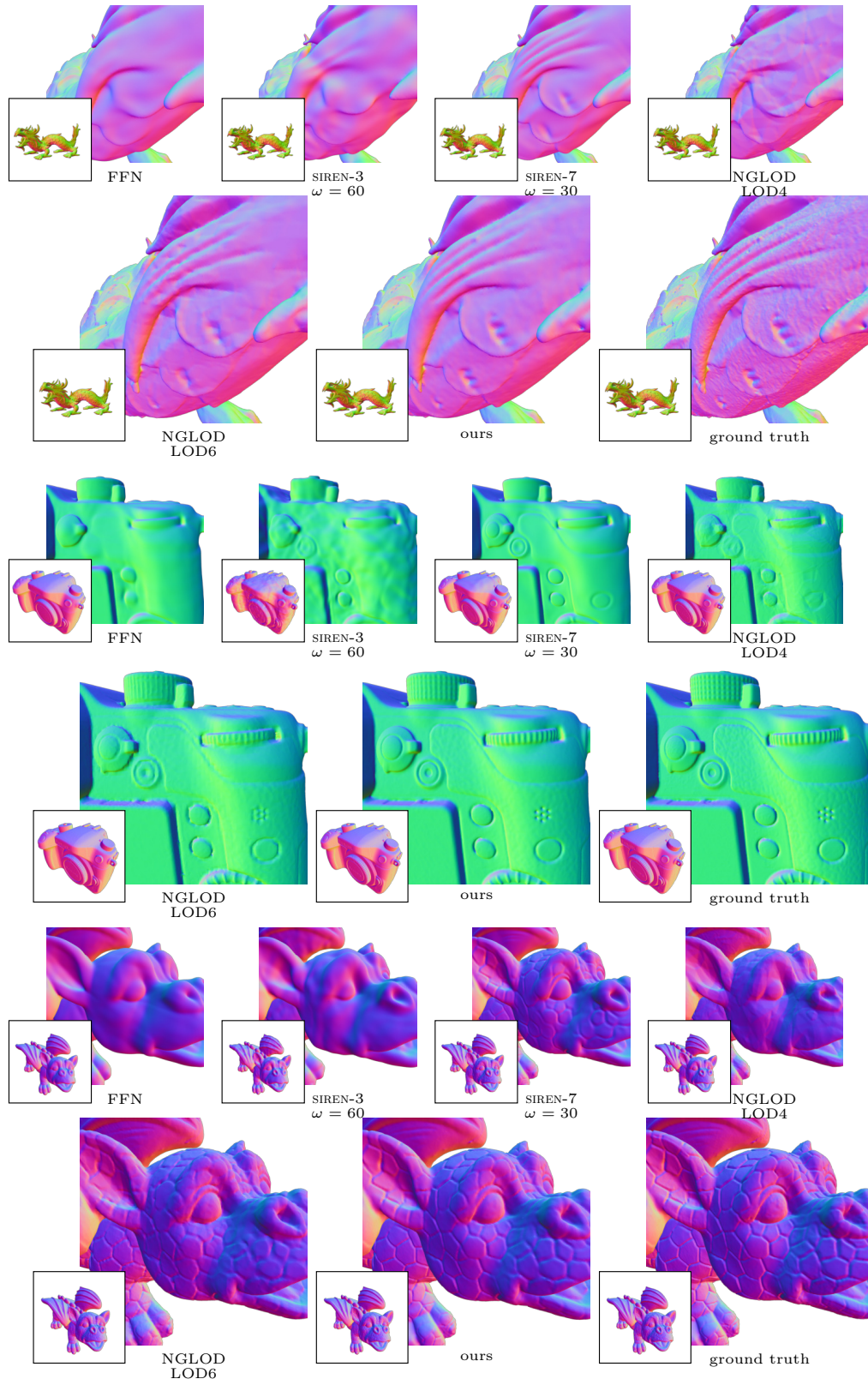


Figure 12: Comparison of detail reconstruction (better viewed with zoom-in). Methods that did not converge are omitted in the visual comparison.

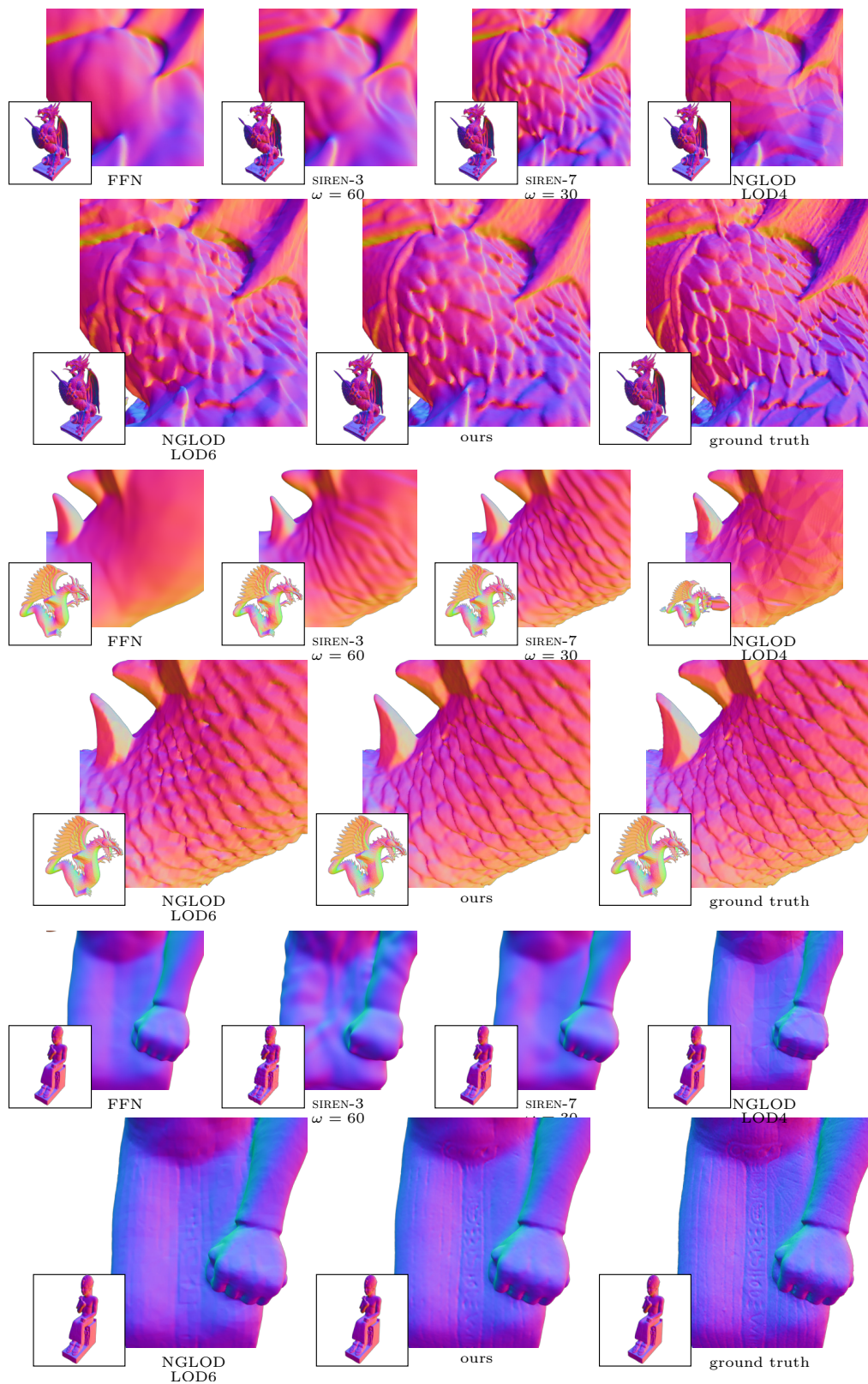


Figure 12: ((Continued) Comparison of detail reconstruction (better viewed with zoom-in)

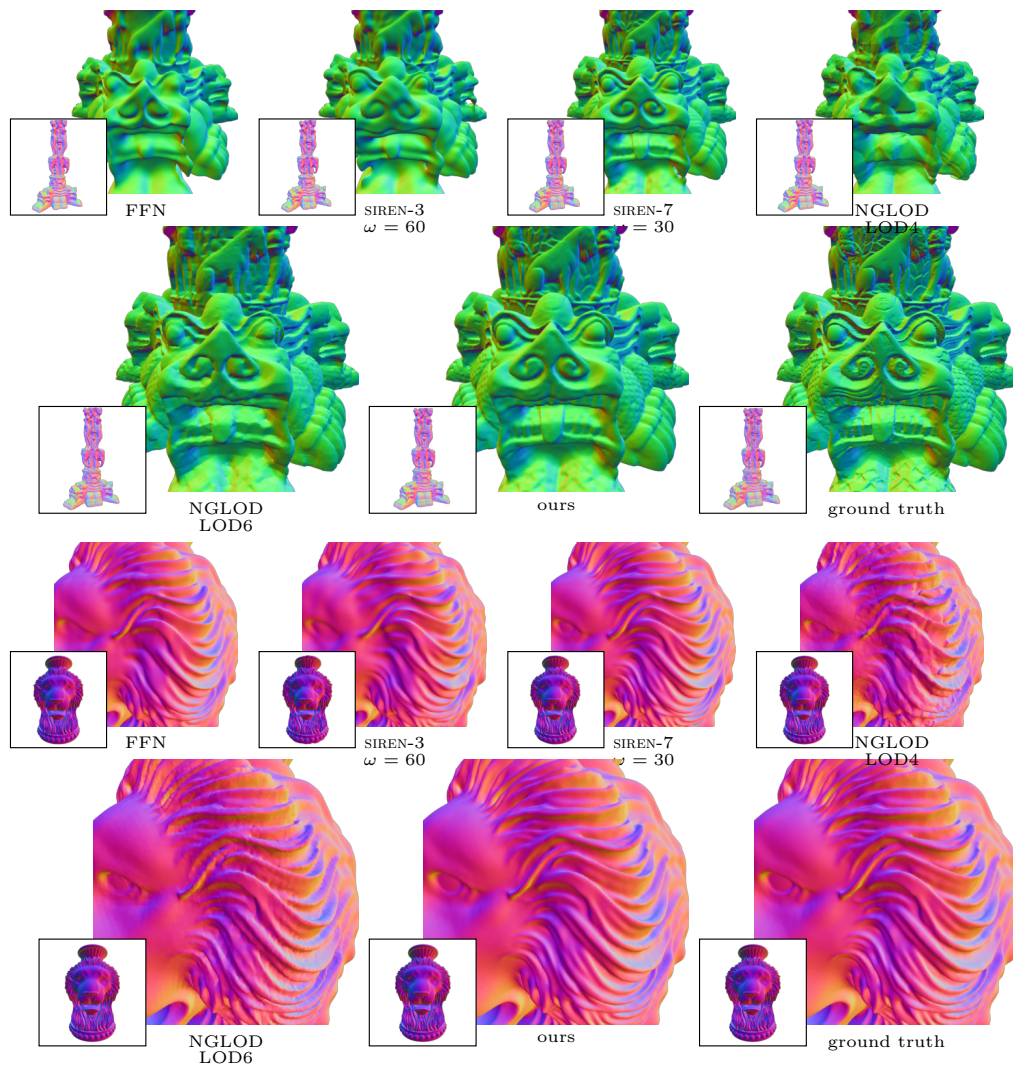


Figure 12: ((Continued) Comparison of detail reconstruction (better viewed with zoom-in)